World Scientific
www.worldscientific.com

Effect of annealing temperature on structural and magnetic properties of strontium hexaferrite nanoparticles synthesized by sol–gel auto-combustion method

Ebrahim Roohani[*,‡], Hadi Arabi[†], Reza Sarhaddi[*],
Saeedeh Sudkhah[*] and Ameneh Shabani[*]

[*]*Magnetism and Superconducting Research Laboratory,
Department of Physics, University of Birjand, Iran*
[†]*Department of Physics, Faculty of Science,
Ferdowsi University of Mashhad, Mashhad, Iran*
[‡]*ebrahimroohani@yahoo.com*

In this paper, strontium hexaferrite nanoparticles were synthesized by the sol–gel auto-combustion method. Effect of annealing temperature on crystal structure, morphology and magnetic properties of nanoparticles was investigated by X-ray diffraction (XRD), Fourier transform infrared (FT-IR), transmission electron microscopy (TEM) and vibrating sample magnetometer (VSM). Also, the thermal decomposition of as-synthesized powdered samples has been studied by thermogravimetric analysis (TGA). The XRD patterns confirmed the formation of single phase M-type hexagonal crystal structure for powders annealed above $950°$C, whereas the presence of hematite (α-Fe_2O_3) as secondary phase was also observed for sample annealed at $900°$C. Furthermore, the crystallinity along with the crystallite size were augmented with annealing temperature. Comparison of the FT-IR spectra of the samples before and after annealing treatment showed the existence of metal–oxygen stretching modes after annealing. The thermogravimetric analysis confirmed the thermal decomposition of as-burnt powders happened in three-stage degradation process. The TEM images showed the nanoparticles like hexagonal-shaped platelets as the size of nanoparticles increases by increasing the annealing temperature. With increasing annealing temperature, the magnetic saturation and the coercivity were increased to the maximum value of 74.26 emu/g and 5.67 kOe for sample annealed at $1000°$C and then decreased.

[‡]Corresponding author.

1. Introduction

M-type hexagonal ferrites are important permanent magnetic materials widely studied since their discovery in the 1950s.[1] Among the hexagonal ferrite materials with general chemical formula $MFe_{12}O_{19}$ (M = Ba, Sr, Pb), strontium ferrite ($SrFe_{12}O_{19}$) possesses a special place due to its appropriate magnetic properties, chemical stability and low cost compared with rare-earth compounds.[2–4] It is a hard magnet with high coercivity, which originates from high magnetocrystalline anisotropy with single easy magnetization axis[5] and is considered as a material with promising scientific and technological applications such as permanent magnets, recording media, telecommunication and as components in microwave, higher-frequency and magneto-optical devices.[6–9]

Strontium hexagonal ferrite can be synthesized by several processes. The conventional way to synthesis Sr-ferrites using the solid state reaction by mixing of oxide/carbonate and then calcined at high temperatures ($> 1200°C$) has some inherent disadvantages such as chemical inhomogeneity, coarser particle size and introduction of impurities during ball milling.[10–13] Thus, the preparation of strontium hexagonal ferrite powder with fine particle size, narrow particle size distribution and minimum particle agglomeration has received considerable attention in order to improve the material properties. Different nonconventional preparation techniques have been employed to synthesize $SrFe_{12}O_{19}$ ferrite including the co-precipitation method,[14,15] hydrothermal method,[16,17] the salt-melting method,[18] mechanical alloying,[19,20] the traditional sol–gel process[2,21,22] and sol–gel auto-combustion method.[23,24] Among these methods, the sol–gel auto-combustion technique (also called low-temperature self-combustion or citrate–nitrate method) has aroused interest because of its utilization of the heat released from the reactions of the hydrocarbon species from the chelating agents with the nitrate oxidant, rapidly producing nanoparticles with a narrow size distribution in a relatively short processing time at a very low temperature.[24,25]

There are many process parameters in wet-chemical methods like the sol–gel auto-combustion process, which can affect the properties of $SrFe_{12}O_{19}$ nanoparticles such as reactant pH, Fe/Sr stoichiometric ratio and annealing temperature. To the best of our knowledge, there is no report in literature to study the annealing temperature effects on physical properties of nanostructured strontium hexaferrite powders synthesized by sol–gel auto-combustion method. Therefore, in this paper, strontium hexaferrite nanoparticles have been synthesized with the Fe/Sr ratio of 12 by a sol–gel auto-combustion method and then the effect of annealing temperature on phase formation, microstructure and magnetic properties of strontium hexaferrite nanopowders have been studied. It was observed

that the different physical properties were changed significantly with the annealing temperature.

2. Experimental

2.1. *Materials*

Iron nitrate pentahydrate (Fe(NO$_3$)$_3$ · 9H$_2$O) and strontium nitrate (Sr(NO$_3$)$_2$) as inorganic reactants, citric acid as complexing agent ammonium hydroxide as a neutralizing agent and double-distilled water as dispersing solvent were used to prepare strontium hexaferrite nanoparticles. All starting precursors were of high-purity compounds.

2.2. *Preparation by sol–gel auto-combustion method*

In this work, SrFe$_{12}$O$_{19}$ strontium hexaferrite nanoparticles were synthesized by sol–gel auto-combustion method as follows: The starting precursors (Fe(NO$_3$)$_3$ · 9H$_2$O, Sr(NO$_3$)$_2$; Fe/Sr = 12) with a stoichiometric amount of metal nitrates were dissolved in double-distilled water by stirring on a hotplate at 50°C. The temperature was increased to 70°C and then citric acid was subsequently added to solution (molar ratio of total metal ions and citric acid in the solution is 1:1) and the resulting mixture was stirred for 30 min. Then, the pH was adjusted to about 7 by adding ammonium hydroxide. Aqueous suspensions were stirred and heated for several hours at 80°C until a highly viscous gel was produced. In the final step of the sol–gel auto-combustion process, the obtained gel is allowed to burn via auto-combustion reaction and then was dried at 250°C for 1 h. Finally, the burnt product which has a tree-like structure (Fig. 1) was grounded and then annealed at different temperature (900, 950, 1000 and 1050°C) for 5 h with a heating rate of 5°C/min to remove any organic residue and form the hexaferrite phase.

Fig. 1. (Color online) Tree-like structure (dendritic stucture) of strontium hexaferrite powders after auto-combustion and before any annealing treatment.

2.3. *Powders characterization*

Thermogravimetric analysis (TGA) was done on the dried precursor in air with a heating rate of 5°C/min on the Shimadzu TA-50WSI TGA instrument. Fourier transform infrared (FT-IR) spectra for as-burnt powders were recorded on a Shimadzu FTIR 4300 spectrometer. The X-ray diffraction (XRD) patterns of powders, prepared at various annealing temperatures, were recorded by the D8 Advance Bruker system using Cu-K$_\alpha$ radiation ($\lambda = 0.154056$ nm) with 2θ ranging from 25 to 70°. Transmission electron microscopy (TEM) images were obtained using a LEO 912 AB system operating at 120 kV. A vibrating sample magnetometer (VSM, Lake Shore 7400) was used to measure the magnetic properties at room temperature.

3. Results and Discussion

3.1. *Thermal analysis*

Figure 2 shows the thermal decomposition characteristics of an unannealed powder of SrFe$_{12}$O$_{19}$ (dried and as-burnt powder at $T = 250$°C). As can be seen, the TG curve exhibits three stages of weight loss. The first stage of weight loss, $\approx 5\%$ appears between room temperature to 230°C, is attributed to the evaporation of coordinated and solvent water. This is also related to the complete chelation process with the loss of NO$_x$ gaseous. The second stage of weight loss ($\approx 20\%$) occurs in range 230–550°C. The major weight loss resulting from the decomposition of
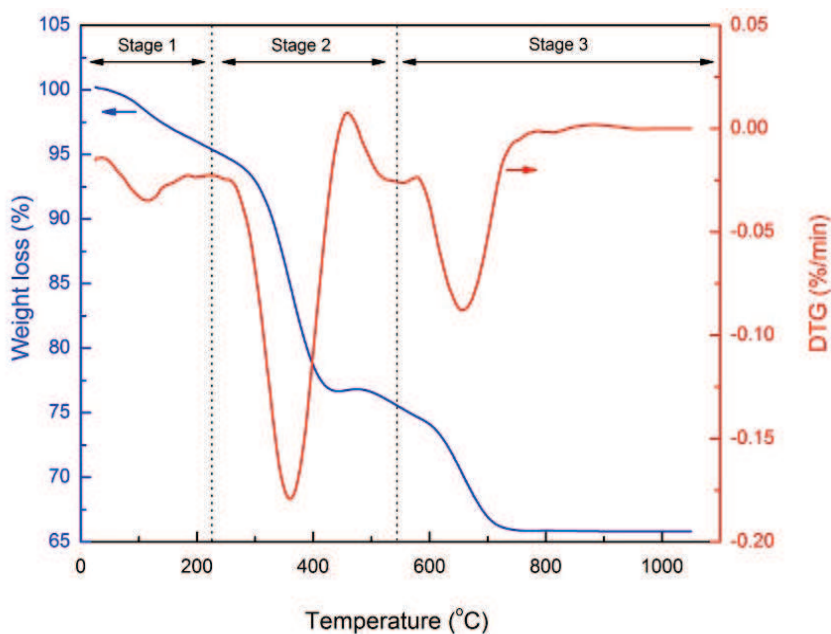

Fig. 2.   (Color online) TG/DTG curve of as-burnt SrFe$_{12}$O$_{19}$ powder.

residual oxidizer (nitrates) and the organics (i.e., citric acid) in the precursors resulting in the sharp exothermic peak in DTG curve (at $T = 360°$C). Such behavior may be due to the oxidation and decomposition process of unreacted carboxyl metal group and nitrate group remaining after combustion result in the liberation of gases such as H_2O, CO_x and NO_x.[26,27] Two observed peaks (at $T = 655$ and $850°$C) in the last stage of thermal decomposition are attributed to the transformation of hydroxides to oxides and formation of strontium spinel ferrite ($SrFe_2O_4$) and strontium hexaferrite ($SrFe_{12}O_{19}$), respectively.[28,29] Above $900°$C, no further distinguishable weight loss was detected indicating the elimination of all organic constituents. According to this schema, we have annealed the samples at different temperatures above $900°$C to evaluate the effects of annealing temperature on physical properties of $SrFe_{12}O_{19}$ powders.

3.2. *FT-IR analysis*

The FT-IR spectra of strontium hexaferrite powders before and after annealing are shown in Fig. 3. Data analysis on the FT-IR spectrum of as-burnt powder ($T = 250°$C) indicates that the characteristic bands peaking at 1618, 1444 and 875 cm^{-1} originate from the light absorption corresponding to the anti-symmetric carboxyl group stretching vibration, anti-symmetric NO_3^{-1} stretching and bending
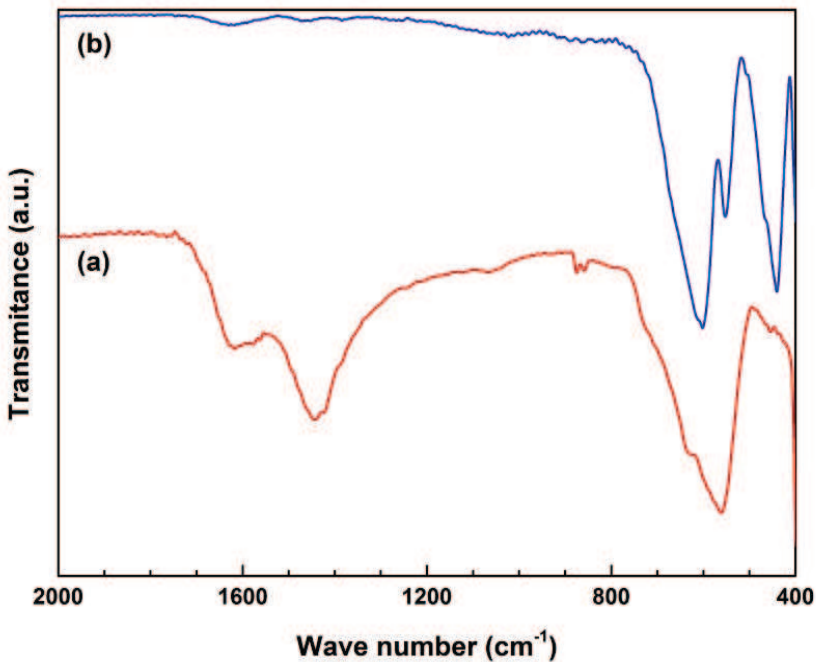

Fig. 3. (Color online) FT-IR spectra of (a) as-burnt at $T = 250°$C and (b) annealed at $T = 900°$C $SrFe_{12}O_{19}$ samples.

vibration, respectively.[30,31] There is also a notable absorption near 562 cm^{-1} which are corresponded to metal complexes.[32] After annealing of the sample at 900°C, no peaks have been observed corresponding to the citric acid ($C_6H_8O_7$), which confirms the complete combustion of citric acid. Furthermore, three signature absorption peaks at bands at 449, 552 and 601 cm^{-1} appear which are due to the metal–oxygen stretching vibrations of hexaferrite.[3,33] The peak at 449 cm^{-1} indicates A_{2u} vibration of octahedral FeO_6 bonds and other two peaks indicate E_{1u} vibration of FeO_4 tetrahedral.[34,35] Moreover, the peaks at 449 and 601 cm^{-1} are intense whereas the peak at 552 cm^{-1} is similar to a small notch. Similar behavior was observed by Durmus *et al.* for barium hexaferrite.[36] Together with the results from the TG/DTG analysis, now we can conclude that the organic compounds were eliminated above 900°C and bonds between metals and oxygen were formed.

3.3. *XRD analysis*

Figure 4 presents the XRD patterns of $SrFe_{12}O_{19}$ powders annealed at different temperature. As can be seen, the main phase for all temperatures has M-type hexagonal structure with space group P6$_3$/mmc (No. 194) and matches well with the JCPDS card (#33–1340, $a = 5.8866$ Å and $c = 23.037$ Å).[37] A small amount of intermediate phase, α-Fe_2O_3 is observed for the powders annealed at 900°C which

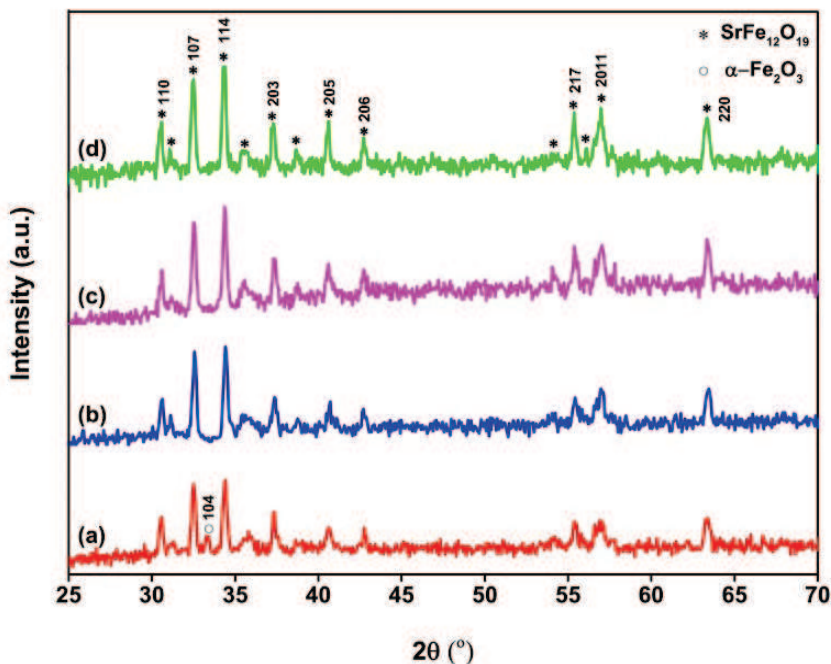Fig. 4.   (Color online) XRD patterns for Sr-ferrite powders annealed at various temperatures for 5 h in air: (a) 900°C, (b) 950°C, (c) 1000°C and (d) 1050°C.

indicates that annealing at 900°C was not quite enough to obtain single phase hexagonal crystal structure. The secondary phase disappeared completely when the sample was annealed at 950°C at which the crystallinity was enhanced to form single phase SrFe$_{12}$O$_{19}$.

Various structural parameters including lattice parameters ("a" and "c"), cell volume (V) and crystallite size (D) are calculated using the following formulae[38,39]:

$$\frac{1}{d^2} = \frac{4}{3}\left(\frac{h^2 + hk + k^2}{a^2}\right) + \frac{l^2}{c^2}\,, \tag{1}$$

$$V = \frac{\sqrt{3}}{2}a^2 c\,, \tag{2}$$

$$D = \frac{0.9\lambda}{\beta\cos\theta}\,, \tag{3}$$

where "d" is the interplanar distance, h, k, l are the Miller indices, λ is the wavelength of the incident X-ray beam, θ is the diffraction angle and β presents the full-width half maximum of the Bragg peak corrected using the corresponding peak in micron-sized powder (pure silicon) as follows:

$$\beta^2 = \beta_{\text{obs.}}^2 - \beta_{\text{inst.}}^2\,, \tag{4}$$

where $\beta_{\text{obs.}}$ and $\beta_{\text{inst.}}$ are the observed peak broadening of Sr-ferrite and the half-width of the standard material in radians. The obtained results are listed in Table 1.

When the annealing temperature is increased, the lattice parameters and therefore cell volume were increased as follows: The a-axis lattice parameter increases from 5.8476 to 5.8695 Å, an increase of 0.0219 or 0.37%. At the same time, the c-axis lattice parameter increases from 22.8925 to 23.0562 Å, an increase of 0.1637 or 0.72%. These results show an anisotropic expansion of the unit cell that also recently reported for BaFe$_{12}$O$_{19}$ hexagonal ferrites.[40,41] Furthermore, according to Verstegen and Stevels,[42] an examination of c/a ratio can be used to quantify the structure type, as the M-type structure can be assumed if the ratio is observed to be lower than 3.98. As shown in Table 1, the c/a ratios were calculated for the samples ranged from 3.915 to 3.928, well within the ratio range of M-type structures. On the other hand, with increasing annealing temperature, the intensity of peaks, specially [114] peak, is found to increase which demonstrate an improvement in the degree of crystallinity of the annealed powders at further temperate. It can also be

Table 1. Structural parameters of SrFe$_{12}$O$_{19}$ powders annealed at different temperatures.

Annealing temperature (°C)	a(Å)	c(Å)	c/a	Volume (Å^3)	Crystallite size (nm)
900	5.8476	22.8925	3.9148	677.921	26
950	5.8563	22.9551	3.9197	681.799	35
1000	5.8637	23.0126	3.9246	685.235	48
1050	5.8695	23.0562	3.9281	687.892	63

observed that the crystallite size of Sr-ferrite increased with increasing annealing temperature. This increase is mainly due to coalescence of neighboring particles. In other words, at higher temperature, the atoms have sufficient thermal energy to move into stable position, leading to the increase of the intensity of peaks, decrease of β values and therefore an increment in crystallite size.[43,44]

3.4. *TEM analysis*

Figure 5 shows the TEM images of the $SrFe_{12}O_{19}$ powders annealed at $T = 900$ and 1050°C. As can be seen, most of the grains are like platelets having sharp grain boundaries which are also observed for $BaFe_{12}O_{19}$ and $PbFe_{12}O_{19}$ hexaferrites.[40,45] Besides, a close look at these images might provide hindsight of the hexagonal texture of some grains, a characteristic of the hexagonal crystal structure of the M-type hexaferrites $MFe_{12}O_{19}$ (M = Ba, Sr, Pb). The average grain size measured by TEM was found about 80 and 98 nm, respectively for 900 and 1050°C. Increasing of annealing temperature leads to a larger degree of crystal growth, resulting in bigger grains.

3.5. *Magnetic analysis*

Magnetization curves of the $SrFe_{12}O_{19}$ powders annealed at various temperatures are shown in Fig. 6. The magnetic parameters such as saturation magnetization (M_s), remanence (M_r) and coercivity field (H_c) as a function of annealing temperature are listed in Table 2. It should be noted, since all samples do not show the saturated magnetization despite high magnetic field (20 kOe), therefore, the saturation magnetization values are estimated from the extrapolating of M versus $1/H$ curves when $1/H$ goes to zero.[46]
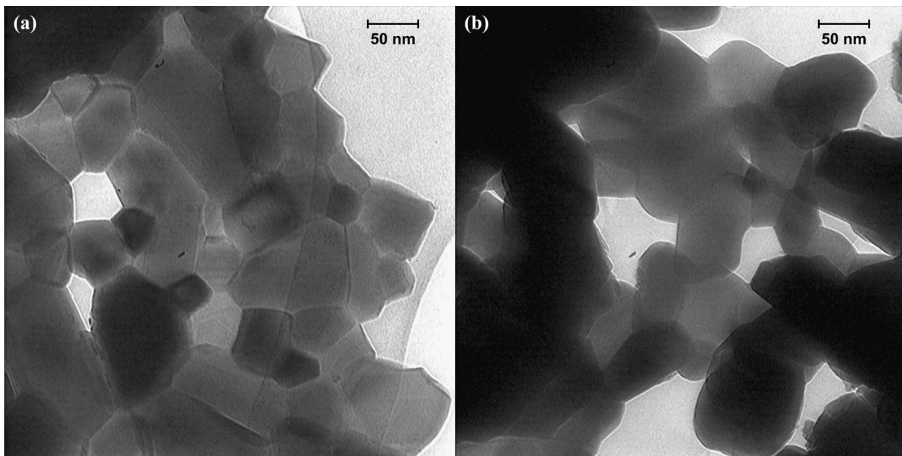

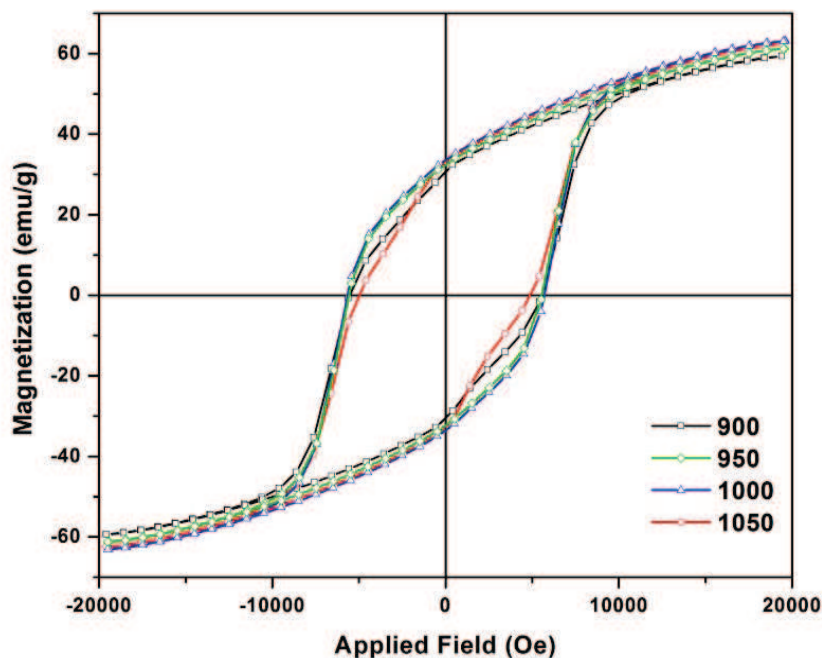Fig. 5.   TEM images of $SrFe_{12}O_{19}$ powders annealed at (a) 900°C and (b) 1050°C.

Fig. 6. (Color online) Room temperature M–H loop of the $SrFe_{12}O_{19}$ powders annealed at different temperatures.

Table 2. Magnetic parameters of $SrFe_{12}O_{19}$ powders annealed at different temperatures.

Annealing temperature (°C)	M_r (emu/g)	M_s (emu/g)	H_c (Oe)
900	30.55	70.53	5532
950	32.37	72.79	5572
1000	33.50	74.26	5672
1050	32.79	73.81	4918

The values of both M_s and M_r for the powders annealed at 900°C is relatively lower than other temperatures. This is due to the existence of a small amount of the paramagnetic intermediate phase α-Fe_2O_3 which lowers the saturation and remanent magnetization as well.[4,40] However, with increasing annealing temperature, the magnetic saturation was increased which could be mainly due to the elimination of Fe_2O_3 phase, improvement of phase quality and increase of particle size.[41] As identified in previous sections, increasing annealing temperature resulted in the higher average grain size, so that the amount of superparamagnetic particles in the sample decreases, thus allowing an increase in the overall magnetization.[47] In addition, in accordance with the core-shell magnetic morphology,[48,49] the nanoparticles consisted of ferrimagnetically aligned core spins and a surface spin disordered layer (magnetically dead layer). Accordingly, the higher core/shell ratio for large

nanoparticles led to elimination of surface effects and consequently, enhancement of magnetization. Besides, the saturation magnetization values are lower than the bulk value ($M_s = 92.6$ emu/g)[14] which is principally due to the large surface area of nanoparticles and the incomplete coordination of atoms at the particle surface, leading to a noncollinear spin configuration, which reduces the magnetization of small particles.[50] On the other hand, the values of coercivity obtained for samples increased with increment in annealing temperature, reached maximum value of 5672 Oe for sample annealed at 1000°C and then decreased. This could result from transition of the magnetic single-domain (SD) to magnetic multi-domain (MD) structure during growth of the particle size.[41,51]

4. Conclusion

In this paper, the effect of annealing temperature ($T = 900$–1050°C) on structural, morphological and magnetic properties of $SrFr_{12}O_{19}$ nanoparticles prepared by sol–gel auto-combustion method have been studied in detail. The observations from the XRD, TGA, FT-IR, TEM and VSM studies are summarized as follows.

Based on the TGA results, a three-stage degradation process was identified with a heating rate of 5°C/min (S-I: 25–230°C; S-II: 230–550°C; S-III: 550–900°C). The FT-IR spectra of samples after annealing process showed three absorption peaks at bands at 449, 552 and 601 cm^{-1} originated from the metal–oxygen stretching vibrations of strontium hexaferrite. A well-defined single crystalline strontium hexaferrite phase was formed when the annealing temperature was above 950°C. The crystallite size for the produced ferrite was increased, by increasing the temperature, from 26 nm at $T = 900$°C to 63 nm at $T = 1050$°C. The TEM images showed nearly hexagonal platelet shape for strontium ferrite nanoparticles. It is also found that the saturation magnetization and coercivity are both enhanced with increasing annealing temperature to $T = 1000$°C and then decreased.

References

1. J. J. Went *et al.*, *Philips Tech. Rev.* **13**, 194 (1951).
2. P. C. A. Brito *et al.*, *Physica B* **384**, 91 (2006).
3. M. Liu *et al.*, *J. Solid State Chem.* **184** 871 (2011).
4. F. Sánchez-De Jesús *et al.*, *Ceram. Int.* **40**, 4033 (2014).
5. R. C. Pullar, *Prog. Mater. Sci.* **57**, 1191 (2012).
6. J. Dho *et al.*, *J. Magn. Magn. Mater.* **285**, 164 (2005).
7. M. J. Iqbal *et al.*, *J. Magn. Magn. Mater.* **320**, 881 (2008).
8. S. Singhal *et al.*, *World J. Condens. Matter. Phys.* **1**, 101 (2011).
9. H. Z. Wang *et al.*, *J. Alloys Compds.* **537**, 43 (2012).
10. D. H. Chen and Y. Y. Chen, *Mater. Res. Bull.* **37**, 801 (2002).
11. H. How, X. Zuo and C. V. Wave, *IEEE Trans. Magn.* **41**, 2349 (2005).
12. M. Radwan, M. M. Rashad and M. M. Hessien, *J. Mater. Process. Technol.* **181**, 106 (2007).
13. D. Seifert *et al.*, *J. Am. Ceram. Soc.* **94**, 2109 (2011).
14. M. M. Hessien *et al.*, *J. Alloys Compds.* **476**, 373 (2009).

15. A. Ataie and S. Heshmati-Manesh, *J. Eur. Ceram. Soc.* **21**, 1951 (2001).
16. M. Jean *et al.*, *J. Alloys Compds.* **496**, 306 (2010).
17. A. Xia *et al.*, *J. Magn. Magn. Mater.* **332**, 186 (2013).
18. Z. B. Guo *et al.*, *J. Magn. Magn. Mater.* **175**, 333 (1997).
19. W. A. Kaczmarek, B. Idzikowski and K. H. Muller, *J. Magn. Magn. Mater.* **177**, 921 (1998).
20. S. V. Ketov *et al.*, *J. Magn. Magn. Mater.* **300**, 479 (2006).
21. A. Ghasemi and A. Morisako, *J. Magn. Magn. Mater.* **320**, 1167 (2008).
22. T. M. H. Dang *et al.*, *Adv. Nat. Sci. Nanosci. Nanotechnol.* **3**, 025015 (2012).
23. Z. Zhang *et al.*, *J. Alloys Compds.* **525**, 114 (2012).
24. S. M. Mirkazemi, S. Alamolhoda and Z. Ghiami, *J. Supercond. Novel Magn.* **28**, 1543 (2015).
25. A. Sutka and G. Mezinskis, *Front. Mater. Sci.* **6**, 128 (2012).
26. N. A. Abdullah *et al.*, *Int. J. Electrochem. Sci.* **7**, 9401 (2012).
27. A. Mali and A. Ataie, *J. Alloys Compds.* **399**, 245 (2005).
28. M. J. Iqbal and M. N. Ashiq, *Chem. Eng. J.* **136**, 383 (2008).
29. V. N. Dhage *et al.*, *J. Alloys Compds.* **509**, 4394 (2011).
30. S. H. Xiao *et al.*, *Mater. Chem. Phys.* **106**, 82 (2007).
31. S. M. Masoudpanah and S. A. Seyyed Ebrahimi, *Thin Solid Films* **520**, 199 (2011).
32. W. Zhang *et al.*, *Appl. Surf. Sci.* **257**, 176 (2010).
33. M. Sivakumar, A. Gedanken and W. Thong, *J. Magn. Magn. Mater.* **268**, 182 (2004).
34. M. V. Rane, D. Bahadur and C. M. Srivastava, *J. Phys. D: Appl. Phys.* **32**, 2001 (1999).
35. W. Zhao *et al.*, *J. Am. Ceram. Soc.* **90**, 2095 (2007).
36. Z. Durmus *et al.*, *Nano–Micro Lett.* **3**, 108 (2011).
37. G. B. Teh, Y. C. Wong and R. D. Tilley, *J. Magn. Magn. Mater.* **323**, 2318 (2011).
38. M. N. Ashiq, M. J. Iqbal and I. Gul, *J. Magn. Magn. Mater.* **323**, 259 (2011).
39. R. Sarhaddi *et al.*, *Physica E* **43**, 452 (2010).
40. M. A. Ahmed, N. Helmy and S. I. El-Dek, *Mater. Res. Bull.* **48**, 3394 (2013).
41. Z. Mosleh *et al.*, *Ceram. Int.* **40**, 7279 (2014).
42. J. M. P. J. Verstegen and A. L. N. Stevels, *J. Lumin.* **9**, 406 (1974).
43. G. Wicks *et al.*, *Materials Challenges in Alternative and Renewable Energy II: Ceramic Transactions* (John Wiley & Sons, New York, 2013).
44. M. Sobri *et al.*, *Superlattices Microstruct.* **70**, 82 (2014).
45. S. M. Ramay *et al.*, *J. Nanomater.* **2014**, 452468 (2014).
46. Z. Durmus, *J. Nanomater.* **2014**, 302350 (2014).
47. M. J. Iqbal *et al.*, *J. Alloys Compds.* **500**, 113 (2010).
48. K. L. Krycka *et al.*, *Phys. Rev. Lett.* **104**, 207203 (2010).
49. H. B. Na, I. C. Song and T. Hyeon, *Adv. Mater.* **21**, 2133 (2009).
50. A. Kale, S. Gubbala and R. D. K. Misra, *J. Magn. Magn. Mater.* **277**, 350 (2004).
51. M. S. E. Shafie *et al.*, *J. Mater. Sci., Mater. Electron.* **25**, 3787 (2014).